Temperature and excitation energy dependence of Raman scattering in the nodal-line semimetal $ZrAs_2$

R. Bacewicz,[1,*] C. Jastrzębski,[1] K. Zberecki,[1] A. S. Wadge,[2] D. Jastrzębski,[2,3] and A. Wiśniewski[2,4]

[1]*Faculty of Physics, Warsaw University of Technology, Koszykowa 75, PL- 00–662, Warsaw, Poland*

[2]*International Research Centre MagTop, Institute of Physics, Polish Academy of Sciences, Aleja Lotnikow 32/46, PL-02-668 Warsaw, Poland*

[3]*Faculty of Chemistry, Warsaw University of Technology, Noakowskiego 3, 00-664 Warsaw, Poland*

[4]*Institute of Physics, Polish Academy of Sciences, Aleja Lotnikow 32/46, PL-02-668 Warsaw, Poland*

(Received 15 May 2024; revised 8 July 2024; accepted 14 August 2024; published 27 August 2024)

We present a Raman study of $ZrAs_2$ single crystals, a nodal-line semimetal with symmetry-enforced Dirac-like band crossings. We identified the symmetry of phonon modes by polarized light measurements and comparison with calculated phonon frequencies. Significant dependence of peak intensities on the excitation wavelength was observed, indicating quantum interference effects. Phonon peaks in the spectra were superimposed on the electronic background, with quasielastic scattering observed for the 785-nm excitation. The temperature dependence of phonon peaks' linewidth indicates that the electron-phonon coupling plays an essential role in phonon decay.

DOI: 10.1103/PhysRevB.110.054114

I. INTRODUCTION

Topological semimetals have attracted considerable scientific interest in recent years owing to their unique electronic structure and the specific role of symmetry. In most Dirac and Weyl semimetals, the energy bands intersect at a point in k space. Nodal-line semimetals exhibit band crossings that extend on a one-dimensional line or loop in k space [1]. The nonsymmorphic symmetries can play an important role in protecting the crossings [2,3]. Transition-metal dipnictides ZrP_2 [4] and $ZrAs_2$ [5] have been found to represent nodal-line semimetals. Bannies *et al.* [4], using angle-resolved photoemission spectroscopy (ARPES) and magnetotransport studies, found that ZrP_2 exhibited an extremely large and unsaturated magnetoresistance (MR) of up to 40 000% at 2 K, which originated from an almost perfect electron-hole compensation. Their band-structure calculations and ARPES studies showed that ZrP_2 hosted a topological nodal loop in proximity to the Fermi level. Very recently, magnetotransport studies of $ZrAs_2$ have been reported by Nandi *et al.* [6]. They observed large MR with quadratic-field dependence, unsaturated up to magnetic field of 14 T. Their electronic structure analysis demonstrated the coexistence of electron- and hole pockets at the Fermi surface. The carrier concentration was estimated from the field-dependent Hall resistivity, and it was found that the charge carriers were nearly compensated, which resulted in a large MR. Wadge *et al.* [5], reported results for the $ZrAs_2$ single crystals, obtained using ARPES technique and density-functional theory (DFT) calculations. In ARPES scans, a distinctive nodal-line structure was observed at photon energies of 30 and 100 eV. Furthermore, DFT calculations unveiled symmetry-enforced band crossings anchored at specific points in the Brillouin zone.

Raman-scattering studies of topological semimetals offer insight into lattice dynamics, electronic structure, and electron-phonon interaction [7–10]. This paper presents the Raman study of zirconium diarsenide $ZrAs_2$ single crystals. We performed angle-resolved polarization measurements to assign symmetry to the observed Raman modes. With the support of the phonon frequencies' *ab initio* calculations, it was possible to identify all Raman modes in $ZrAs_2$. The Raman spectra depend substantially on the excitation energy, with some modes visible only for specific excitation. We ascribe this to resonance-like–interference effects related to the complicated band structure of $ZrAs_2$. We also analyzed the electronic Raman scattering, which produced a pronounced continuum background in the Raman spectra. An essential aspect of the Raman spectroscopy of semimetals is the role of electron-phonon coupling. Our study shows the electron-phonon coupling effects in $ZrAs_2$, manifesting in the temperature dependence of Raman peaks linewidth.

II. EXPERIMENTAL DETAILS

$ZrAs_2$ crystallizes in the $PbCl_2$-type structure with the centrosymmetric, nonsymorphic space group *Pnma* (D_{2h}^{16}, *International Tables for Crystallography* No. 62). Orthorhombic cell parameters are [11] $a = 6.8006$ Å, $b = 3.6883$ Å, and $c = 9.0328$ Å. The unit cell of $ZrAs_2$ contains 4 formula units (Fig. 1); all atoms occupy 4c Wycoff positions. Needlelike crystals of $ZrAs_2$ have been grown by the iodine transport method, with the crystallographic b axis along the needle length. The chains of covalently bonded As atoms along the b axis provided preferred direction of crystal growth [11].

Raman measurements were performed on two spectrometers: HORIBA Jobin Yvon Aramis spectrometer with 2400-l/mm diffraction grating (approximate resolution 1 cm^{-1}), used for measurements with 473- and 633-nm excitation lasers; and Renishaw Quanta spectrometer with diffraction

*Contact author: rajmund.bacewicz@pw.edu.pl

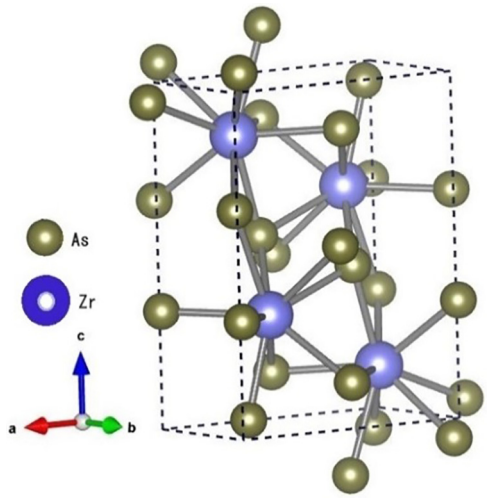

FIG. 1. Orthorhombic unit cell of $ZrAs_2$.

grating 1800 l/mm and approximate resolution of 2 cm^{-1} (785-nm laser). The beam power was kept low in all cases to prevent sample heating. The spectra were measured in the temperature range 80 − 443 K.

Raman spectra were measured in backscattering geometry with parallel ($\hat{e}_i||\hat{e}_s$) and crossed ($\hat{e}_i \perp \hat{e}_s$) configurations, where $\hat{e}_i$, $\hat{e}_s$ were polarization vectors of incident and scattered light, respectively. For most of the measurements the natural (101) face of the crystal was used, with light impinging along the Z' axis, perpendicular to the (101) face (Fig. 2). We use Porto's notation throughout the paper, e.g., $Z'(YY)\bar{Z}'$ configuration, which we write in short as (YY).

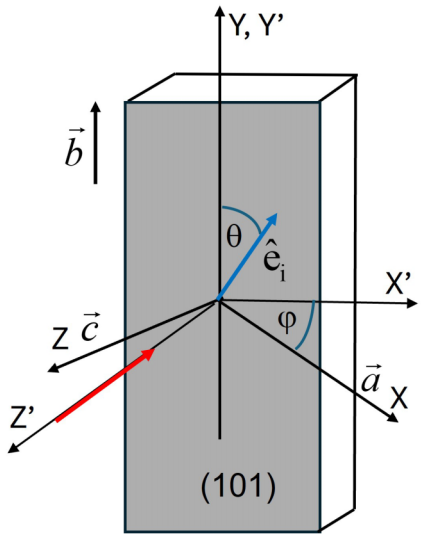

FIG. 2. Experiment geometry and crystal orientation. The crystal frame of reference (XYZ) and the lab frame of reference $(X'Y'Z')$. Unit-cell vectors $\boldsymbol{a}$, $\boldsymbol{b}$, and $\boldsymbol{c}$ are shown. Light polarization (incident and scattered) is in the $(X'Y)$ plane. The red arrow shows the light-propagation vector, and the blue denotes the light-polarization vector. The angle between X and X' axes is $\varphi = 53.0247°$.

Computational details

The calculations of the band structure were performed within density-functional theory (DFT) as implemented in the VASP package [12–15] with projector augmented-wave pseudopotentials [16,17]. In all cases, the Perdew-Burke-Ernzerhof generalized gradient approximation functional [18] was used. For the sampling of the Brillouin zone, a dense 8 × 8 × 8 grid was used, while the plane-wave energy cutoff was set to 500 eV. All the structures were optimized until the force exerted on each atom was smaller than 10^{-5} eV/Å. Phonon-dispersion calculations were made using, the frozen-phonon method as implemented in the PHONOPY code [19].

III. RESULTS AND DISCUSSION

A. Room-temperature studies

According to the nuclear site group analysis [20] of $ZrAs_2$ structure (see Supplemental Material [21] for details), 18 Raman-active optical vibrational modes at zero wave vector are distributed as follows:

$$\Gamma = 6A_g + 3B_{1g} + 6B_{2g} + 3B_{3g}. \tag{1}$$

Because $ZrAs_2$ has a centrosymmetric structure, only even-symmetry modes are allowed in Raman spectra. The Raman tensors for these modes are

$$A_g = \begin{pmatrix} a & 0 & 0 \\ 0 & b & 0 \\ 0 & 0 & c \end{pmatrix}$$

$$B_{1g} = \begin{pmatrix} 0 & d & 0 \\ d & 0 & 0 \\ 0 & 0 & 0 \end{pmatrix}$$

$$B_{2g} = \begin{pmatrix} 0 & 0 & e \\ 0 & 0 & 0 \\ e & 0 & 0 \end{pmatrix}$$

$$B_{3g} = \begin{pmatrix} 0 & 0 & 0 \\ 0 & 0 & f \\ 0 & f & 0 \end{pmatrix}. \tag{2}$$

Figure 3 presents room-temperature Raman spectra recorded at the (YY) geometry for three excitation energies: 2.62 eV (473 nm), 1.96 eV (633 nm), and 1.58 eV (785 nm), with continuous background dependent on excitation energy. The background in spectra will be discussed further below. Phonon-mode positions, linewidths, and intensities were analyzed after background subtraction. Generally, the Raman spectra measured in this study are consistent with selection rules stemming from the Raman tensor. However, some residual intensity peaks corresponding to the modes forbidden for a given polarization are present due to resonant conditions. Apparent difference is observed for the lowest-frequency A_g mode at 94.5 cm^{-1}, which has a significant intensity in the forbidden cross-polarizer configuration (Fig. 4).

Table I assigns the observed phonon modes according to their symmetry compared with calculated frequencies (VASP_FP). The polarized angular-resolved Raman spectra confirm this assignment. Polar graphs for selected modes as a function of the θ angle between the incident light polariza-

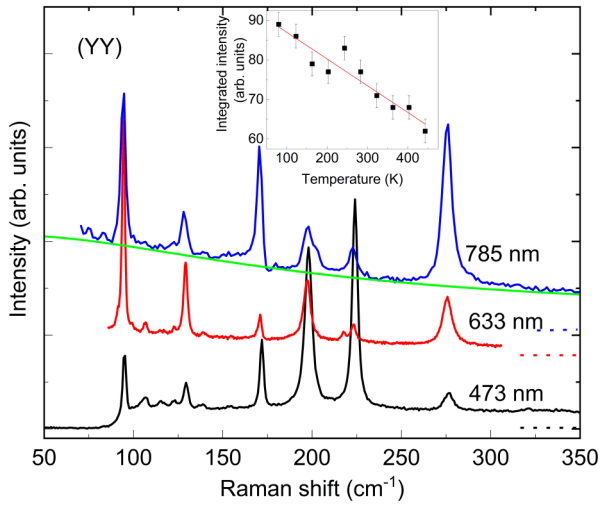

FIG. 3. Room-temperature Raman spectra for three different excitations (as measured). The continuous background is present with the dashed lines as reference levels for every plot. The green line is the fitted model of quasielastic scattering background using expression (3) to the 785-nm plot. The inset shows the temperature dependence of the integrated background intensity for the 785-nm excitation.

tion vector and the b axis are presented and analyzed in the Supplemental Material [21].

Figure 5 shows room-temperature spectra for (YY) and ($X'X'$) polarization for different excitation wavelengths. Intensities of several Raman peaks have distinctive excitation wavelength dependence. The A_g symmetry modes at 129 and 171 cm^{-1} have much higher intensity for the 633- and 785-nm excitations than for the 473-nm excitation. The A_g mode at 276 cm^{-1} does not appear in the 473-nm spectrum. Mode at 244 cm^{-1} (B_{2g}) is the most intense for the 473-nm excitation

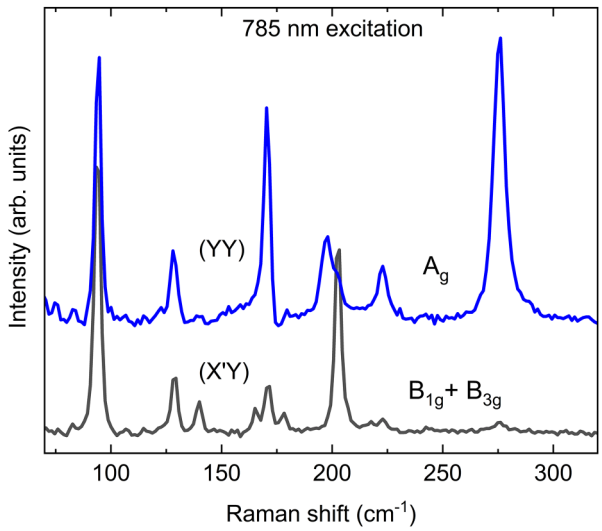

FIG. 4. Comparison of the parallel (YY) and the ($X'Y$) crossed-polarization spectra recorded with the 785-nm excitation at room temperature (the electronic background subtracted).

TABLE I. Symmetry assignment of the observed Raman modes in $ZrAs_2$. The mode frequencies were determined from the room-temperature spectra. Accuracy of mode-frequency values is approximately 1 cm^{-1}. Theoretical values were calculated using the DFT method.

	Frequency (cm^{-1})		
	Experiment	Theory (VASP FP)	Symmetry assignment
1	94.5	87.8	A_g
2		89.8	B_{1g}
3	129	121.9	A_g
4	140	134.5	B_{3g}
5	149	137.3	B_{2g}
6	166	154.2	B_{3g}
7	171	161.2	A_g
8	173.5	164.4	B_{2g}
9	178	170.1	B_{1g}
10	182.5	173.6	B_{2g}
11	197	186.5	A_g
12	203	193.9	B_{3g}
13	207	195.3	B_{2g}
14	217	206.4	B_{1g}
15	223	210.9	A_g
16		211.7	B_{2g}
17	244	232.2	B_{2g}
18	276	261.0	A_g

in the ($X'X'$) configuration and appears as a small kink in the 785-nm spectrum (it is not present for the 633-nm excitation).

Usually, in resonant Raman spectra, all modes are seen to increase their intensity when the excitation energy is close to a characteristic electronic transition (Van Hove singularity or band nesting). In the Raman spectra of $ZrAs_2$, we observe both resonance and antiresonance effects depending on mode. This means that different electronic intermediate states are involved in the Raman scattering. Since in the band structure of $ZrAs_2$ [Fig. 6(a)] many bands are available for such transitions, different bands in the whole Brillouin zone take part in the light-scattering process. It leads to a quantum interference effect, when electronic transitions in different parts of the Brillouin zone enhance or quench each other [23–26]. Due to the complicated band structure of $ZrAs_2$, we cannot identify the regions that contribute constructively to the Raman amplitude and those that interfere destructively. It is worth noting that differences in electron-phonon matrix elements for phonon modes can also account for observed excitation dependence [26].

As shown in Fig. 3, the continuous background is present in the $ZrAs_2$ Raman-scattering spectra. The background shows a quasielastic scattering (QES) wing and a flat finite-energy continuum extending up to 1500 cm^{-1}. It is polarization dependent and has the highest intensity in the (YY) configuration, i.e., for light polarization along the b axis, where arsenic atoms form covalently bonded chain. It also depends on excitation energy and has the highest intensity with an intense QES part for the lowest-used excitation energy of 1.58 eV (785 nm). For the higher excitation energies, 1.96 and 2.62 eV, the intensity of the quasielastic component is weaker, and the

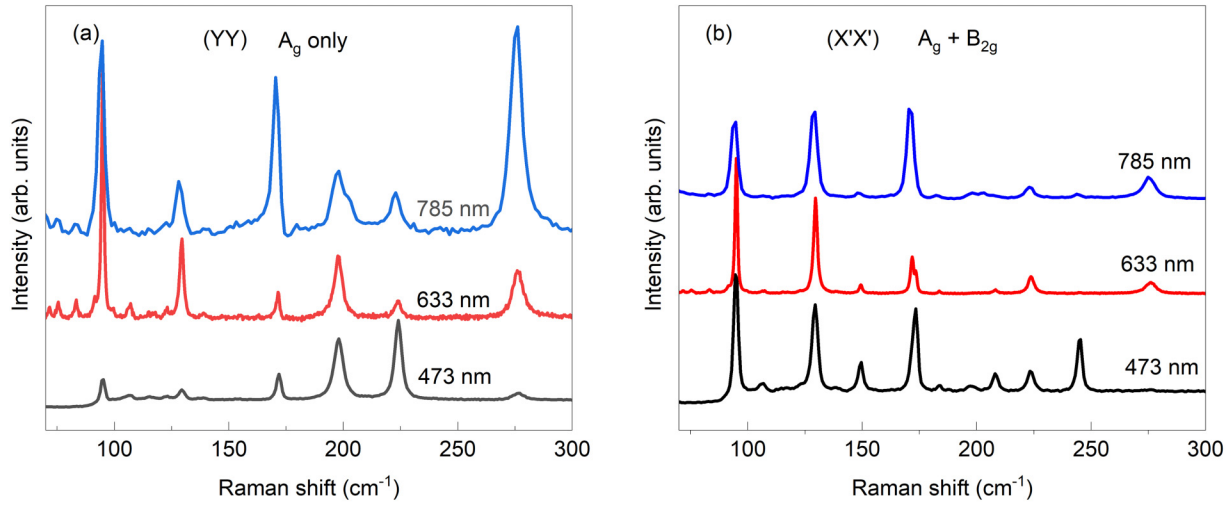

FIG. 5. Room-temperature Raman spectra in the (YY) (a) and $(X'X')$ (b) configurations for 473, 633, and 785-nm excitation wavelengths, respectively. The (YY) spectra were normalized to the 197-cm^{-1} peak and $(X'X')$ to 129-cm^{-1} peak.

broad energy range background is observed. The background intensity measured with the 785-nm excitation decreases with increasing temperature (inset in Fig. 3).

A broad band of continuous energy Raman scattering was observed for some topological semimetals: e.g., in Cd_3As_2 [7,27], WP_2 [28], and LaAlSi [23]. It is attributed to electronic Raman scattering due to electron density fluctuations. Such a background was first observed in heavily doped semiconductors [29,30]. It was interpreted as scattering by intervalley density fluctuations in the collision-limited regime [31]. Zawadowski and Cardona [32] have shown that in Raman spectra of metals a background can be due to a scattering between different parts of Fermi surface. Intense QES is also observed in the metallic phase of $La_{0.7}Sr_{0.3}MnO_3$ [33]. The quasielastic part of the continuum background is often described by the Lorentzian profile for zero energy:

$$I_R \propto (n(\omega)+1)\frac{\omega\Gamma_{el}}{\omega^2+{\Gamma_{el}}^2}, \tag{3}$$

where $n(\omega)$ is the Bose factor, and Γ_{el} is the width of the Lorentz profile.

Equation (3) gives a good fit to the QES wing in the 785-nm excitation spectra (Fig. 3). The intensity of this background decreases with temperature in the range of $80-443$ K (inset in Fig. 3). Γ_{el} is almost independent of temperature and has an average value of (230 ± 20) cm^{-1}.

Due to the presence of an electronic background in Raman-scattering spectra, one can expect the effects of interference between discrete phonon modes and electron continuum states, resulting in asymmetric Fano-type profiles of Raman peak intensity. However, we did not isolate any peaks in the spectra with undoubtedly a Fano-type line shape. The lack of Fano peaks in Raman spectra of $ZrAs_2$ resembles the situation of another topological semimetal TaAs, where the electron-phonon coupling was identified in temperature evolution of the Raman modes' linewidth, but no asymmetric Fano-like Raman peaks were reported [34]. However, asymmetric Fano profiles have been found in the infrared spectra of TaAs [35].

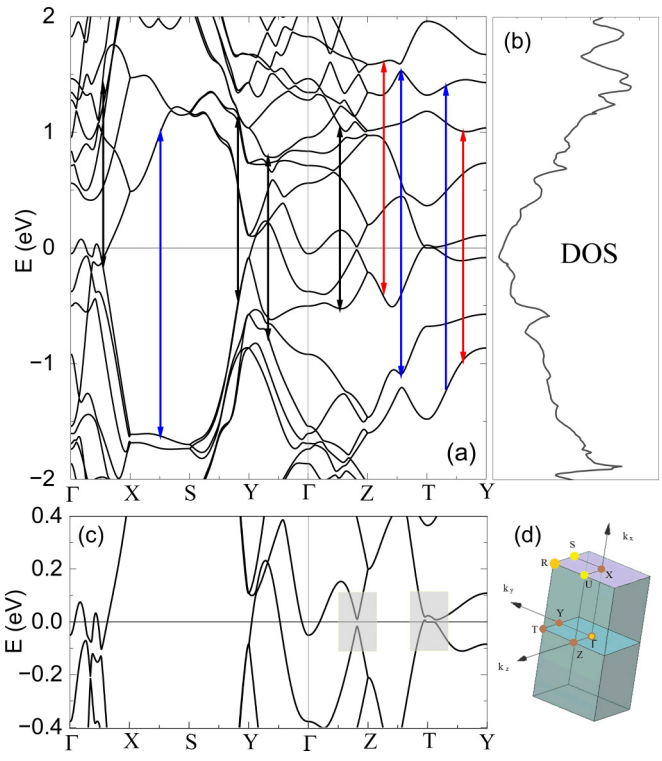

FIG. 6. (a) Band structure of $ZrAs_2$ with a few allowed electronic transitions to/from intermediate states in the Raman process, which are shown with the vertical arrows: black: 785-nm excitation, red: 633 nm, and blue: 473 nm; (b) Density of states; (c) Details of the electronic bands close to the Fermi level; shaded areas indicate regions of the Brillouin zone where phonon decay via e-h pairs excitation is energetically possible; and (d) Brillouin zone of $ZrAs_2$.

B. Effect of temperature on Raman scattering in $ZrAs_2$

Figure 7 shows the evolution of the Raman spectra measured in the parallel configuration for $\theta = 45°$ in the temperature range $80-443$ K for the 2.62-eV (473-nm)

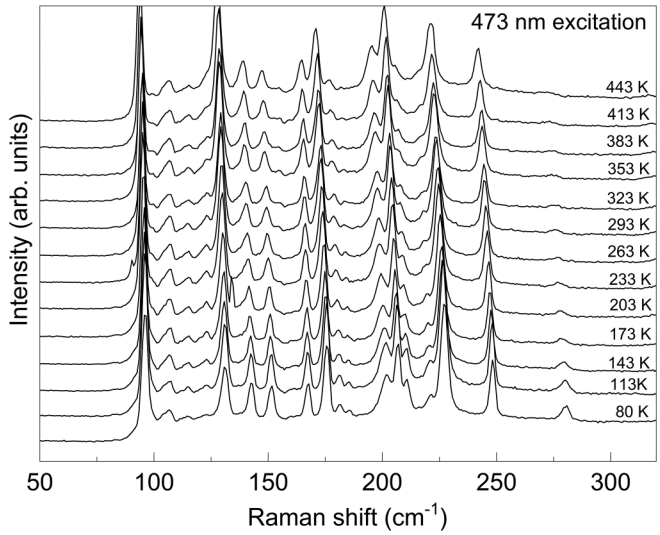

FIG. 7. Temperature dependence of the Raman spectra measured with the 473-nm excitation for parallel configuration and $\theta = 45°$ (for the 633-nm excitation see the Supplemental Material [21]).

excitation. Most peaks are visible for the whole temperature range. However, some peaks for the 2.62-eV excitation lose their intensity with increasing temperature, e.g., the A_g mode at 280 cm^{-1} (at 80 K) is hardly visible for temperatures above 300 K. Temperature dependence of the Raman spectra for the 1.96-eV (633-nm) excitation is shown in Fig. S3 in the Supplemental Material [21].

To find the basic parameters of the phonon lines (position, linewidth, and area) the fitting procedure was performed. The best fit was achieved with the pseudo-Voigt function, which is a weighted sum of the Lorentz and Gaussian profiles. Attempts to fit spectra with the Voigt profile gave unreliable results because of too-low signal-to-noise ratio [36].

The temperature dependence of the optical phonon frequency and linewidth is usually ascribed to two effects: quasiharmonic effect due to thermal expansion of the crystal lattice, and the anharmonic effect due to the phonon-phonon coupling. The first effect is often approximated by a linear dependence:

$$\omega(T) = \omega_0 + \chi T \tag{4}$$

Anharmonic interaction is analyzed within the extended Klemens model [37,38], which assumes that phonon decays into two or three acoustic phonons. The change of phonon frequency is given as

$$\Delta\omega_{\text{anh}}(T) = A\left(1 + \frac{2}{e^x - 1}\right) + B\left(1 + \frac{3}{e^y - 1} + \frac{3}{(e^y - 1)^2}\right), \tag{5}$$

where $\hbar\omega$ is phonon energy, $x = \hbar\omega/2k_BT$, $y = \hbar\omega/3k_BT$ and A and B denote anharmonic constants related to three phonon processes (decay of optical phonon into two phonons) and four phonon processes, respectively.

Left panels in Fig. 8 present the temperature dependence of the position of several phonon peaks in $ZrAs_2$. In the tem-

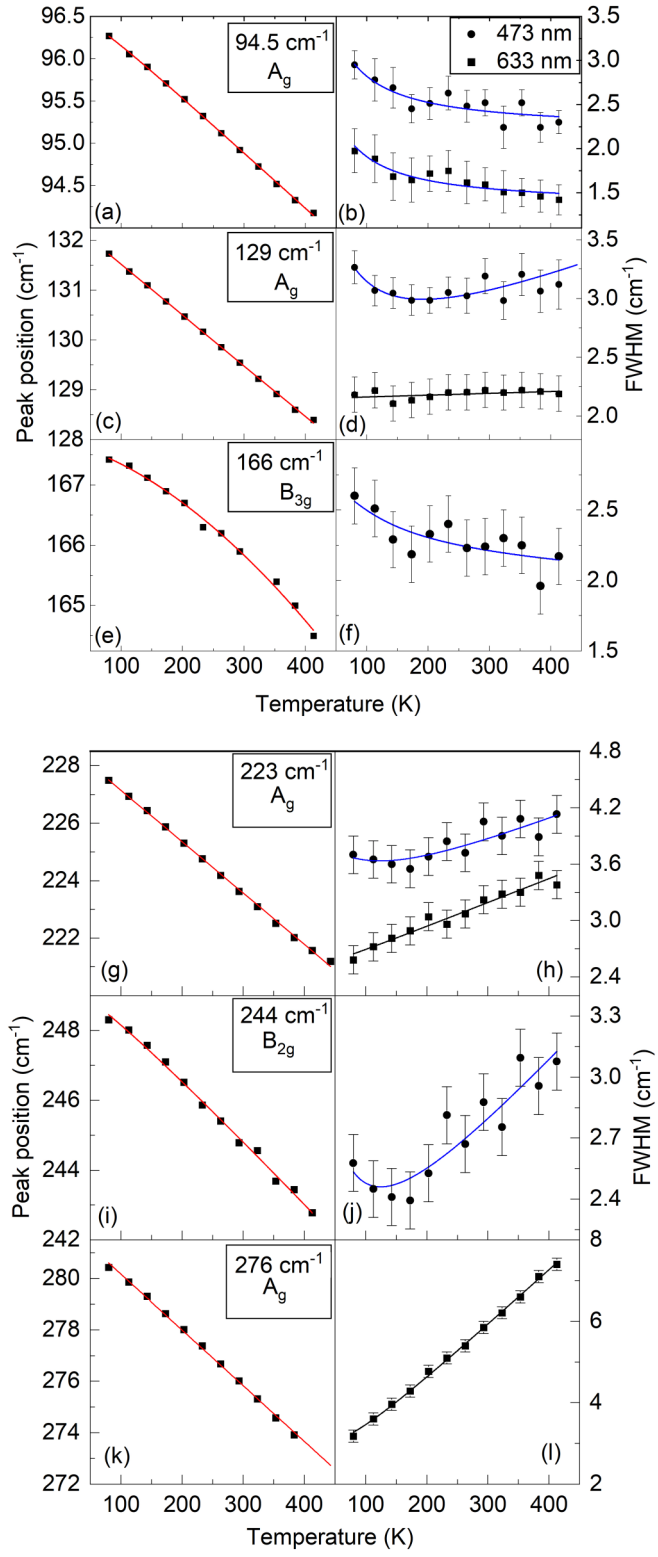

FIG. 8. Temperature dependence of phonon-mode frequency in $ZrAs_2$ (left panels) and the linewidth (right panels) for two excitation wavelengths: 473 and 633 nm. The red line is a fit of the expression (5) to the mode-frequency change. In the right panels, blue line is a fit of the model where both anharmonic effects and electron-phonon interaction are included. The black line corresponds to the linewidth model of anharmonic interaction only (6). The linewidth results were not corrected for the instrumental broadening.

TABLE II. Fitting parameters of the temperature dependence of peak position and linewidth: the redshift linear dependence parameter χ (for the modes at 166- and 245-cm^{-1} nonlinear dependence was observed); parameter C corresponds to an anharmonic Klemens model of the thermal evolution of the linewidth, and γ_{eph} to the electron-phonon coupling process for the 473-nm excitation. Additionally, for the 94.5-cm^{-1} mode, parameters from the fit for the 633-nm excitation spectra are given.

Mode frequency (cm^{-1})	Symmetry	χ (cm^{-1}/K)	C (cm^{-1})	γ_{eph} (cm^{-1})
94.5 (473 nm)	A_g	−0.0064	0	1.86 ± 0.03
94.5 (633 nm)	A_g	−0.0064	0	1.68 ± 0.02
129	A_g	−0.01	0.1 ± 0.03	1.7 ± 0.5
166	B_{3g}		−0.01	0.62 ± 0.5
223	A_g	−0.018	0.21 ± 0.06	0.65 ± 0.05
244	B_{2g}		0.32 ± 0.08	0.8 ± 0.5
276	A_g	−0.022	1.36 ± 0.12	0

perature range used in our experiment, the redshift of phonon frequency is linear function of temperature for most modes, with a slight deviation at temperatures near 80 K. The fitted values of the χ parameter are given in Table II. However, it is worth noting that the anharmonic expression (5) also produces almost a straight-line fit to our data, so the effects of lattice expansion and anharmonicity are practically indistinguishable. The temperature redshift of phonon frequency for the modes at 166 and 244 cm^{-1} is distinctly nonlinear and follows the expression (5).

Similar expression to the anharmonic redshift of phonon frequency (5) describes the temperature evolution of the phonon linewidth due to the anharmonic interaction:

$$\Gamma_{\text{anh}}(T) = C\left(1 + \frac{2}{e^x - 1}\right) + D\left(1 + \frac{3}{e^y - 1} + \frac{3}{(e^y - 1)^2}\right). \tag{6}$$

It predicts an increase in linewidth with increasing temperature. However, several phonon modes in Raman spectra of $ZrAs_2$ show a reduction in linewidth for increasing temperature (right panels in Fig. 8). It is due to important contribution of the electron-phonon coupling, which is particularly important in semimetals. In this interaction phonons decay into electron-hole pairs via intra- or interband transitions close to the Fermi level (E_F) [8,39,40]. Temperature dependence of the linewidth is determined by the difference in occupation of electronic states below and above E_F. For increasing temperature, the occupation of the electron states below E_F decreases, while the occupation of the states above E_F increases. It leads to decreasing number of available electronic states for the phonon-induced transitions and results in a decrease of the linewidth with increasing temperature. This behavior is quantitively expressed by the formula [39,40]

$$\Gamma_{\text{eph}} = \gamma_{\text{eph}}[(f(-\hbar\omega/2) - (f(\hbar\omega/2)], \tag{7}$$

where $f(\hbar\omega) = (\exp(\hbar\omega/k_BT) + 1)^{-1}$ is the Fermi-Dirac distribution function, and γ_{eph} is the electron-phonon coupling parameter.

It is worth noting that taking into account a finite chemical potential in (7) can result in a nonmonotonic temperature dependence of Γ_{eph} [8,34].

The decay of optical phonon with zero wave vectors via the creation of the electron-hole pairs depends on the energy and symmetry of phonon mode. Since the highest-energy phonons at the center of the Brillouin zone of $ZrAs_2$ have an energy of 34 meV, electron-phonon coupling is possible for pairs of electron bands below and above the Fermi energy, which are closer to each other than 34 meV. It can happen only with an electron k vector along the Γ - Z line and around the T point in the Brillouin zone [Fig. 6(c)]. However, symmetry-based selection rules (with and without spin-orbit coupling) do not allow Raman-active phonons to induce interband transitions at the T point. Due to spin-orbit coupling, such transitions are allowed near the T point and along the Γ - Z line. We cannot exclude that conditions for effective electron-phonon coupling may also exist at general k points in the Brillouin zone.

In an analysis of the temperature dependence of the linewidth, we used an expression with two contributions: anharmonic term Γ_{anh} [Eq. (6)] (we set $D = 0$, since four-phonon processes give negligible contribution), and the electron-phonon coupling term Γ_{eph} according to the expression (7).

$$\Gamma = \Gamma_0 + \Gamma_{\text{anh}} + \Gamma_{\text{eph}}. \tag{8}$$

We investigated the temperature dependence of the linewidth of phonon peaks represented by the full width at half maximum for two excitation energies, 1.96 eV (633 nm) and 2.61 eV (473 nm), whenever the peak was present and measurable in the spectra for a given excitation energy. For low-intensity modes and overlapping peaks it was impossible to get reliable values of the linewidth. Temperature dependence of the linewidth measured for the two excitations exhibited significant differences (Fig. 8). In the spectra recorded with 633-nm laser we observe for most modes almost linear linewidth increase in accord with anharmonic model, apart from the 94.5-cm^{-1} mode, when the 633-nm plot follows the 473-nm line. It is unclear to us what the source of these discrepancies is; one of the possible reasons can be a difference in light-penetration depth for the used excitation energies. For the 473-nm excitation, the contribution of the electron-phonon interaction to phonon decay is seen for several modes as a monotonous decrease or a minimum in the temperature dependence of the linewidth. This type of temperature dependence is observed for the modes of A_g symmetry at 94.5, 129, and 223 cm^{-1}, respectively, for two modes of B_{2g} symmetry at 150 and 244 cm^{-1}, and the 166-cm^{-1} B_{3g} mode. The dominance of the electron-phonon coupling over anharmonic decay is observed for the modes at 94.5 and 166 cm^{-1}, where no contribution from the anharmonic term is

needed ($C = 0$) to fit the experimental data. This observation indicates no clear-cut correlation between the strength of the electron-phonon coupling in phonon decay, and phonon symmetry or frequency. It is an individual property of the phonon mode.

The values of the γ_{eph} parameter, characterizing the strength of electron-phonon coupling for phonon modes (Table II), are smaller than the values reported for some phonon modes in $NiTe_2$: 5.41 cm^{-1} [41] and $PdTe_2$: 28.8 cm^{-1} [42] as well as in graphene and graphite: approximately 10 cm^{-1} [38]. Still, the electron-phonon coupling plays a significant role in phonon decay processes in $ZrAs_2$.

IV. CONCLUSIONS

We have investigated Raman scattering in a Dirac nodal-line semimetal $ZrAs_2$. Raman spectra have been recorded for several excitation laser energies at different light polarizations. The calculated zero wave-vector phonon frequencies and polarization dependence of the Raman peaks enabled symmetry identification of all observed phonon modes. Due to an interference between excitation paths with different intermediate states, significant peak-intensity differences exist for different excitation wavelengths. The polarization-dependent electronic background is present in the Raman spectra, with an intense quasielastic scattering in the spectra recorded with the 785-nm excitation. Effects of electron-phonon interaction manifest themselves in decreasing peak linewidth with increasing temperature for modes of different symmetry, indicating differences in the electron-phonon coupling. We identified points in the Brillouin zone at the Fermi level where optical phonons can decay via e-h pair creation: only for the electronic states on the Γ - Z high-symmetry line and in the vicinity of the T point, are phonons allowed to create e-h pairs. Since in $ZrAs_2$ there are no Dirac points close to the Fermi energy, it is hard to expect a significant influence of these points on the electron-phonon coupling.

ACKNOWLEDGMENTS

This research was partly supported by the Foundation for Polish Science project "MagTop," Project No. FENG.02.01-IP.05–0028/23 cofinanced by the European Union from the funds of Priority 2 of the European Funds for a Smart Economy Program No. 2021–2027 (FENG).

[1] A. Leonhardt, M. M. Hirschmann, N. Heinsdorf, X. Wu, D. H. Fabini, and A. P. Schnyder, Symmetry-enforced topological band crossings in orthorhombic crystals: Classification and materials discovery, Phys. Rev. Mater. **5**, 124202 (2021).

[2] X. Zhou, C.-H. Hsu, H. Aramberri, M. Iraola, C.-Y. Huang, J. L. Mañes, M. G. Vergniory, H. Lin, and N. Kioussis, Novel family of topological semimetals with butterflylike nodal lines, Phys. Rev. B **104**, 125135 (2021).

[3] J. Wang, H. Yuan, Z.-M. Yu, Z. Zhang, and X. Wang, Coexistence of symmetry-enforced phononic Dirac nodal-line net and three-nodal surfaces phonons in solid-state materials: Theory and materials realization, Phys. Rev. Mater. **5**, 124203 (2021).

[4] J. Bannies, E. Razzoli, M. Michiardi, H.-H. Kung, I. S. Elfimov, M. Yao, A. Fedorov, J. Fink, C. Jozwiak, A. Bostwick, E. Rotenberg, A. Damascelli, and C. Felser, Extremely large magnetoresistance from electron-hole compensation in the nodal-loop semimetal ZrP_2, Phys. Rev. B **103**, 155144 (2021).

[5] A. S. Wadge, K. Zberecki, B. J. Kowalski, D. Jastrzebski, P. K. Tanwar, P. Iwanowski, R. Diduszko, A. Moosarikandy, M. Rosmus, N. Olszowska, and A. Wisniewski, Emergent impervious band crossing in the bulk in topological nodal line semimetal $ZrAs_2$ Phys, Rev. B **110**, 035142 (2024).

[6] S. Nandi, B. B. Maity, V. Sharma, R. Verma, V. Saini, B. Singh, D. Aoki, and A. Thamizhavel, Magnetotransport and Fermi surface studies of a purported nodal line semimetal $ZrAs_2$, Phys. Rev. B **109**, 075155 (2024).

[7] A. Sharafeev, V. Gnezdilov, R. Sankar, F. C. Chou, and P. Lemmens, Optical phonon dynamics and electronic fluctuations in the Dirac semimetal Cd_3As_2, Phys. Rev. B **95**, 235148 (2017).

[8] G. B. Osterhoudt, Y. Wang, C. A. C. Garcia, V. M. Plisson, J. Gooth, C. Felser, P. Narang, and K. S. Burch, Evidence for dominant phonon-electron scattering in Weyl semimetal WP_2, Phys. Rev. X **11**, 011017 (2021).

[9] K. Zhang, T. Wang, X. Pang, F. Han, S.-L. Shang, N. T. Hung, Z.-K. Liu, M. Li, R. Saito, and S. Huang, Anisotropic Fano resonance in the Weyl semimetal candidate LaAlSi, Phys. Rev. B **102**, 235162 (2020).

[10] K. Tanaka, T. Nishihara, A. Takakura, Y. Segawa, K. Matsuda, and Y. Miyauchi, Polarized Raman spectroscopy on topological semimetal $Co_3Sn_2S_2$, J. Raman Spectrosc. **54**, 93 (2023).

[11] P. E. R. Blanchard, R. G. Cavell, and A. Mar, On the existence of $ZrAs_2$ and ternary extension $Zr(Ge_xAs_{1-x})As$ ($0 \leqslant x \leqslant 0.4$), J. Alloys Compd. **505**, 17 (2010).

[12] G. Kresse and J. Hafner, *Ab initio* molecular dynamics for liquid metals, Phys. Rev. B **47**, 558(R) (1993).

[13] G. Kresse and J. Hafner, *Ab initio* molecular-dynamics simulation of the liquid-metal−amorphous-semiconductor transition in germanium, Phys. Rev. B **49**, 14251 (1994).

[14] G. Kresse and J. Furthmüller, Efficiency of ab initio total energy calculations for metals and semiconductors using a plane-wave basis set, Comput. Mater. Sci. **6**, 15 (1996).

[15] G. Kresse and J. Furthmüller, Efficient iterative schemes for *ab initio* total-energy calculations using a plane-wave basis set, Phys. Rev. B **54**, 11169 (1996).

[16] P. E. Blöchl, Projector augmented-wave method, Phys. Rev. B **50**, 17953 (1994).

[17] G. Kresse and D. Joubert, From ultrasoft pseudopotentials to the projector augmented-wave method, Phys. Rev. B **59**, 1758 (1999).

[18] J. P. Perdew, K. Burke, and M. Ernzerhof, Generalized gradient approximation made simple, Phys. Rev. Lett. **77**, 3865 (1996).

[19] L. Chaput Togo, T. Tadano, and I. Tanaka, Implementation strategies in phonopy and phono3py, J. Phys.: Condens. Matter **35**, 353001 (2023).

[20] D. L. Rousseau, R. P. Baumann, and S. P. S. Porto, Normal mode determination in crystals, J. Raman Spectrosc. **10**, 253 (1981).

[21] See Supplemental Material at http://link.aps.org/supplemental/10.1103/PhysRevB.110.054114 for details of nuclear site analysis; polarization dependence of Raman intensity; calculated phonon-dispersion curves; and temperature dependence of the Raman spectra for the 633-nm excitation, which includes Ref. [22].

[22] H. B. Ribeiro, M. A. Pimento, C. J. S. de Matos, R. L. Moreira, A. S. Rodin, J. D. Zapata, E. A. T. de Souza, and A. H. Castro Neto, Unusual angular dependence of the Raman response in black phosphorus, ACS Nano **9**, 4270 (2015).

[23] K. Zhang, X. Pang, T. Wang, F. Han, S.-L. Shang, N. T. Hung, A. R. T. Nugraha, Z.-K. Liu, M. Li, R. Saito, and S. Huang, Anomalous phonon-mode dependence in polarized Raman spectroscopy of the topological Weyl semimetal TaP, Phys. Rev. B **101**, 014308 (2020).

[24] H. P. C. Miranda, S. Reichardt, G. Froehlicher, A. Molina-Sanchez, S. Berciaud, and L. Wirtz, Quantum interference effects in resonant Raman spectroscopy of single- and triple-layer $MoTe_2$ from first-principles, Nano Lett. **17**, 2381 (2017).

[25] M. Osiekowicz, D. Staszczuk, K. Olkowska-Pucko, Ł. Kipczak, M. Grzeszczyk, M. Zinkiewicz, K. Nogajewski, Z. R. Kudrynskyi, Z. D. Kovalyuk, A. Patané, A. Babiński, and M. R. Molas, Resonance and antiresonance in Raman scattering in GaSe and InSe crystals, Sci. Rep. **11**, 924 (2021).

[26] I. Abbasian Shojaei, S. Pournia, C. Le, B. R. Ortiz, G. Jnawali, F.-C. Zhang, S. D. Wilson, H. E. Jackson, and L. M. Smith, A Raman probe of phonons and electron–phonon interactions in the Weyl semimetal $NbIrTe_4$, Sci. Rep. **11**, 8155 (2021).

[27] S. Nath Gupta, D. V. S. Muthu, C. Shekhar, R. Sankar, C. Felser, and A. K. Sood, Pressure-induced electronic and structural phase transitions in Dirac semimetal Cd_3As_2: Raman study, EPL **120**, 57003 (2017).

[28] D. Wulferding, P. Lemmens, F. Büscher, D. Schmeltzer, C. Felser, and C. Shekhar, Effect of topology on quasiparticle interactions in the Weyl semimetal WP_2, Phys. Rev. B **102**, 075116 (2020).

[29] M. Chandrasekhar, M. Cardona, and E. O. Kane, Intraband Raman scattering by free carriers in heavily doped *n*-Si, Phys. Rev. B **16**, 3579 (1977).

[30] G. Contreras, A. K. Sood, and M. Cardona, Raman scattering by intervalley carrier-density fluctuations in *n*-type Si: Intervalley and intravalley mechanisms, Phys. Rev. B **32**, 930 (1985).

[31] I. P. Ipatova, A. V. Subashiev, and V. A. Voitenko, Single particle electron light scattering in heavily doped semiconductors, J. Raman Spectrosc. **10**, 221 (1981).

[32] A. Zawadowski and M. Cardona, Theory of Raman scattering on normal metals with impurities, Phys. Rev. B **42**, 10732 (1990).

[33] R. Gupta, A. K. Sood, R. Mahesh, and C. N. R. Rao, Electronic Raman scattering from $La_{0.7}Sr_{0.3}MnO_3$ exhibiting giant magnetoresistance, Phys. Rev. B **54**, 14899 (1996).

[34] J. Coulter, G. B. Osterhoudt, C. A. C. Garcia, Y. Wang, V. M. Plisson, B. Shen, N. Ni, K. S. Burch, and P. Narang, Uncovering electron-phonon scattering and phonon dynamics in type-I Weyl semimetals, Phys. Rev. B **100**, 220301(R) (2019).

[35] B. Xu, Y. M. Dai, L. X. Zhao, K. Wang, R. Yang, W. Zhang, J. Y. Liu, H. Xiao, G. F. Chen, S. A. Trugman, J.-X. Zhu, A. J. Taylor, D. A. Yarotski, R. P. Prasankumar, and X. G. Qiu, Temperature-tunable Fano resonance induced by strong coupling between Weyl fermions and phonons in TaAs, Nat. Commun. **8**, 14933 (2017).

[36] J. Menendez and M. Cardona, Temperature dependence of the first-order Raman scattering by phonons in Si, Ge, and α-Sn: Anharmonic effect, Phys. Rev. B **29**, 2051 (1984).

[37] P. G. Klemens, Anharmonic decay of optical phonons, Phys. Rev. **148**, 845 (1966).

[38] M. Balkanski, R. F. Wallis, and E. Haro, Anharmonic effects in light scattering due to optical phonons in silicon, Phys. Rev. B **28**, 1928 (1983).

[39] M. Lazzeri, S. Piscanec, F. Mauri, A. C. Ferrari, and J. Robertson, Phonon linewidths and electron-phonon coupling in graphite and nanotubes, Phys. Rev. B **73**, 155426 (2006).

[40] N. Bonini, M. Lazzeri, N. Marzari, and F. Mauri, Phonon anharmonicities in graphite and graphene, Phys. Rev. Lett. **99**, 176802 (2007).

[41] M. Theres James, S. Mandal, N. K. Sebastian, P. Mishra, R. Ganesan, and P. S. Anil Kumar, Probing electron-phonon and phonon-phonon coupling in type-II Dirac semi-metal $NiTe_2$ via temperature-dependent Raman spectroscopy, J. Phys.: Condens. Matter **35**, 125701 (2023).

[42] M. M. AL-Makeen, X. Guo, Y. Wang, D. Yang, S. You, M. Yassine, J. Jiang, P.-Bo Song, Y.-G. Shi, H. Xie, J.-Q. Meng, and H. Huang, Investigation of the electron–phonon coupling in Dirac semimetal $PdTe_2$ via temperature-dependent Raman spectroscopy, Phys. Status Solidi RRL **16**, 2200257 (2022).